Journal of Magnetism and Magnetic Materials 424 (2017) 99–107

Contents lists available at ScienceDirect

Journal of Magnetism and Magnetic Materials

journal homepage: www.elsevier.com/locate/jmmm

Magnetic ordering of $Hf_3Ni_2Si_3$-type {Sm, Tb, Er}$_3Co_2Ge_3$ and {Tb, Ho}$_3Ni_2Ge_3$ compounds

A.V. Morozkin[a,*], V.O. Yapaskurt[b], R. Nirmala[c], S. Quezado[d], S.K. Malik[d], Y. Mozharivskyj[e], O. Isnard[f,g]

[a] Department of Chemistry, Moscow State University, Leninskie Gory, House 1, Building 3, Moscow, GSP-1, 119991, Russia
[b] Department of Petrology, Geological Faculty Moscow State University, Leninskie Gory, Moscow 119991, Russia
[c] Indian Institute of Technology Madras, Chennai 600036, India
[d] Departamento de Física Teórica e Experimental, Universidade Federal do Rio Grande do Norte, Natal 59082-970, Brazil
[e] Department of Chemistry and Chemical Biology, McMaster University, 1280 Main Street West, Hamilton, Ontario, Canada L8S 4M1
[f] CNRS, Institut. Néel, 25 rue des Martyrs BP166 x, F-38042 Grenoble, France
[g] Université Grenoble Alpes, Inst. Néel, F-38042 Grenoble, France

ARTICLE INFO

Keywords:
Rare-earth compounds
Magnetic properties
Magnetocaloric effect
Neutron diffraction

ABSTRACT

The magnetic ordering of $Hf_3Ni_2Si_3$-type {Sm, Tb, Er}$_3Co_2Ge_3$ and {Tb, Ho}$_3Ni_2Ge_3$ compounds (space group *Cmcm*, *oC*32) was investigated via magnetization measurements and neutron diffraction study in a zero-applied field. {Sm, Tb, Er}$_3Co_2Ge_3$ and $Ho_3Ni_2Ge_3$ exhibit field sensitive complex antiferromagnetic orderings with T_N=51 K, T_m=10 K for $Sm_3Co_2Ge_3$, T_N=34 K, T_m=13 K for $Tb_3Co_2Ge_3$, T_N=7 K for $Er_3Co_2Ge_3$ and T_N=11 K for $Ho_3Ni_2Ge_3$. At 2 K and above the critical field of ~5 kOe, 20 kOe, 4 kOe and 7 kOe for $Sm_3Co_2Ge_3$, $Tb_3Co_2Ge_3$, $Er_3Co_2Ge_3$ and $Ho_3Ni_2Ge_3$, respectively, saturation magnetizations per rare-earth atom are 6.5 μ_B for $Tb_3Co_2Ge_3$, 7.0 μ_B for $Er_3Co_2Ge_3$ and 8.0 μ_B for $Ho_3Ni_2Ge_3$ in the field of 140 kOe, whereas magnetization of $Sm_3Co_2Ge_3$ has an antiferromagnetic behaviour. The isothermal magnetic entropy change, ΔS_m, indicates a field-induced ferromagnetic ordering in $Sm_3Co_2Ge_3$, Tb_3Co_2Ge3, $Er_3Co_2Ge_3$ and $Ho_3Ni_2Ge_3$ with a maximal ΔS_m value of −10.9 J/kg K for $Ho_3Ni_2Ge_3$ at 11 K for a field change of 50 kOe.

In a zero-applied magnetic field, below T_N=33 K and down to T_m^{ND}=15 K $Tb_3Ni_2Ge_3$ shows an *ac*-antiferromagnetic ordering with the ***C2′/c*** magnetic space group, a $\mathbf{K}_0$=[0, 0, 0] propagation vector and a $a_{Tb3Ni2Ge3}\times b_{Tb3Ni2Ge3}\times c_{Tb3Ni2Ge3}$ magnetic unit cell. Below T_m^{ND}=15 K, its magnetic structure is a sum of the *ac*-antiferromagnetic component with the ***C2′/c*** magnetic space group of the $\mathbf{K}_0$ vector and a sine-modulated *a*-antiferromagnetic component of the $\mathbf{K}_1$=[0, 0, ± 1/3] propagation vector (the magnetic unit cell is $a_{Tb3Ni2Ge3}\times b_{Tb3Ni2Ge3}\times 3c_{Tb3Ni2Ge3}$). The magnetic structure is made from the 'Tb2 - 2Tb1' clusters of the Tb1 8*f* and Tb2 4*c* sublattices with a dominant role of the Tb2 sublattices in the magnetic ordering of $Tb_3Ni_2Ge_3$.

1. Introduction

Structures of many of the rare-earth ternary compounds can be derived from those of the corresponding rare-earth metals through the insertion of transition metals and *p* elements. Besides structural changes, incorporation of the transition metals and *p* elements modifies the magnetic interactions between the rare-earth atoms.

The {Sm, Tb, Er}$_3Co_2Ge_3$ [1] and {Tb, Ho}$_3Ni_2Ge_3$ [2] compounds adopt the $Hf_3Ni_2Si_3$-type structure (ordered variant of Ca_3Ga_5-type one, space group *Cmcm*) [3,4] and they are representatives of $Hf_3Ni_2Si_3$-type {Sc, Y, Gd - Tm, Lu}$_3Fe_2Si_3$, {Sc, Y, Gd - Tm, Lu}$_3Co_2Si_3$ [5–7], {Ce, Nd, Gd}$_3Mn_2Ge_3$ [8,9], {Er, Tm}$_3Fe_2Ge_3$ [10], {Sc, Y, Sm - Tm}$_3Co_2Ge_3$ [1,11–13], {Tm, Lu]$_3Li_2Ge_3$ [14], {Y, Gd - Tm, Lu}$_3Ru_2Ge_3$, {Y, Gd - Tm, Lu}$_3Ir_2Ge_3$ [15–20] and {Y, Tb - Tm, Lu}$_3Ni_2Ge_3$ [2,21,22] rare-earth compounds. The $Hf_3Ni_2Si_3$-type structures can be derived from the Mg-type rare-earth ones via an orthorhombic distortion of the initial hexagonal rare-earth lattice concomitant with the insertion of transition metals and *p* elements. $Hf_3Ni_2Si_3$-type compounds belong to the large family of the two-layer orthorhombic structures with the *Cmcm* space group symmetry [1].

The early reported magnetic measurements on the {Y, Sm, Gd - Tm}$_3Co_2Ge_3$, $Ho_3Ni_2Ge_3$ and $Dy_3Ru_2Ge_3$ compounds indicates their field-sensitive antiferromagnetic nature [1,2,15] and according to the neutron diffraction study in a zero-applied field, $Tb_3Co_2Ge_3$ exhibits an

* Corresponding author.
E-mail address: morozkin@tech.chem.msu.ru (A.V. Morozkin).

http://dx.doi.org/10.1016/j.jmmm.2016.10.036
Received 1 September 2016; Accepted 7 October 2016
Available online 08 October 2016

abc-antiferromagnetic ordering with the $\mathbf{K}_0$=[0, 0, 0], $\mathbf{K}_1$=[± 1/3, 0, 0] and $\mathbf{K}_2$=[1/2, 0, 0] propagation vectors [1].

To understand magnetic features of the orthorhombically distorted rare-earth sublattices in the $Hf_3Ni_2Si_3$-type compounds, magnetic ordering of the {Sm, Tb, Er}$_3Co_2Ge_3$ and {Tb, Ho}$_3Ni_2Ge_3$ compounds was investigated in details in the present work.

2. Experimental details

The {Sm, Tb, Er}$_3Co_2Ge_3$ and {Tb, Ho}$_3Ni_2Ge_3$ samples were prepared by arc-melting the stoichiometric amounts of rare earths (99.9 wt%), Co, Ni (99.95 wt%) and Ge (99.99 wt%). The samples were annealed at 1070 K for 170–240 h in argon atmosphere and subsequently quenched in ice-cold water. The quality of the samples was evaluated using powder X-ray diffraction and microprobe analyses. The X-ray powder data were obtained on the diffractometer Rigaku d/max-2500 (CuK$_\alpha$ radiation, 2θ=5–120 and 10–80°, step 0.02°, 3–6 s/step). An INCA-Energy-350 X-ray EDS spectrometer (Oxford Instruments) on the Jeol JSM-6480LV scanning electron microscope (20 kV accelerating voltage, 0.7 nA beam current and 50 μm beam diameter) was employed for the quantitative microprobe analyses. Signals averaged over three points per phase had estimated standard deviations of 1 at% for rare earth (measured by L-series lines), 1 at% for Co, Ni and Ge (measured by K-series lines).

The magnetization of the polycrystalline samples was measured on a commercial MPMS SQUID magnetometer (Quantum Design) and using the VSM option of the PPMS (Dynacool, Quantum Design) in the temperature range of 2–300 K and applied magnetic fields up to 140 kOe.

Neutron diffraction experiment of $Tb_3Ni_2Ge_3$ was carried out at the high flux reactor of the Institut Laue Langevin (Grenoble, France) using the high flux powder diffractometer D1B operated by the CNRS-CRG team [23]. The diffraction patterns were recorded at several temperatures ranging from 182 K down to 1.5 K. The two axis D1B powder diffractometer used for this work was equipped with a large 1300 cell curved detector which recorded the diffraction pattern over a 2θ range of 130° and the 2θ step of 0.1°. The neutron wavelength of 2.52 Å was selected by the (002) reflection of a pyrolitic graphite monochromator.

The unit cell data of all compounds were derived from the Rietveld analysis of the X-ray powder patterns using the Rietan program [24] in the isotropic approximation and analysis of the unit cell symmetry was done with the aid of the Bilbao Crystallographic Server [25]. The paramagnetic susceptibilities were fitted to the Curie-Weiss law to obtain effective magnetic moments and paramagnetic Weiss temperatures [26]. Magnetocaloric effect (MCE) was calculated in terms of the isothermal magnetic entropy change, ΔS_m, using the magnetization vs field data obtained near the magnetic transition and the thermodynamic Maxwell's equation [27]. Neutron diffraction patterns were identified and calculated using the FULLPROF program in terms of the traditional crystallographic approach [28]. Magnetic space groups [29–31] were used for the analysis of the neutron diffraction patterns.

3. Results

3.1. Crystal structure

The X-ray analysis showed that the {Sm, Tb, Er}$_3Co_2Ge_3$ and $Ho_3Ni_2Ge_3$ samples are single phase and they adopt the $Hf_3Ni_2Si_3$-type structure. Meanwhile, the '$Tb_3Ni_2Ge_3$' sample contained 73 wt% of $Hf_3Ni_2Si_3$-type $Tb_3Ni_2Ge_3$, 20 wt% of TiNiSi-type TbNiGe [3,4] and 7 wt% of CrB-type TbGe [3,4] (Fig. 1s). The refined unit cell data and atomic positions of the $Hf_3Ni_2Si_3$-type compounds are given in Table 1.

The shortest interatomic distances are close to the sum of metallic radii of pure elements [32,33] which indicates a metallic type of bonds in these $Hf_3Ni_2Si_3$-type compounds, e.g. in $Tb_3Ni_2Ge_3$: 0.2970 nm (Tb1-1Ni), 0.3032 nm (Tb2-4Ni), 0.2988 nm (Tb1-2Ge1), 0.2989 nm (Tb1-2Ge2), 0.2941 nm (Tb2-2Ge1), 0.3000 nm (Tb2-2Ge2), 0.3470 nm (Tb1-1Tb2, Tb2-2Tb1), 0.3624 nm (Tb1-1Tb1) (Table 1s). In terms of the interatomic distances, the large Ni-2Ni (0.3730 nm) and Tb2-2Tb2 (0.42027 nm) distances preclude an independent magnetic ordering of these sublattices, whereas Tb2-2Tb1 clusters with the shortest terbium-terbium distance of 0.3470 nm play a crucial role in the magnetic ordering of $Tb_3Ni_2Ge_3$ as in $Tb_3Co_2Ge_3$ [1].

3.2. Magnetic measurements

According to the thermomagnetic measurements, $Sm_3Co_2Ge_3$ shows an antiferromagnetic-type transitions at T_N=51 K and T_m=10 K, $Tb_3Co_2Ge_3$ exhibits transitions at T_N=34 K and T_m=13 K, $Er_3Co_2Ge_3$ and $Ho_3Ni_2Ge_3$ show antiferromagnetic-type transitions at T_N=7 K and T_N=11 K, respectively (Fig. 1). The magnetization of $Er_3Co_2Ge_3$ shows some anomaly at 2 K that could associated with incomplete antiferromagnetic-like transitions around 2 K, whereas magnetization of $Ho_3Ni_2Ge_3$ indicates possible spin-reorientation transitions below 11 K.

Paramagnetic susceptibility of the $Sm_3Co_2Ge_3$ follows the modified

Table 1
Unit cell data of $Hf_3Ni_2Si_3$-type compounds (space group *Cmcm*, N 63, *oC*32, Z=4).

Compound	*a* (nm)	*b* (nm)	*c* (nm)	*V* (nm^3)	R_F (%)	Ref.
$Sm_3Co_2Ge_3$	0.4214	1.0688	1.4173	0.63834		[1]
$Sm_3Co_2Ge_3$[a,b]	0.42186(1)	1.06997(2)	1.41858(3)	0.64032	2.9	This work
$Tb_3Co_2Ge_3$[a]	0.41786(1)	1.05106(2)	1.39728(3)	0.61368	3.6	[1][b]
$Er_3Co_2Ge_3$[a,c]	0.41521(2)	1.03578(3)	1.38015(5)	0.59356	3.3	This work
$Er_3Co_2Ge_3$	0.41487(4)	1.03598(5)	1.38043(8)	0.59330		[1]
$Tb_3Ni_2Ge_3$	0.42002	1.03333	1.4106	0.61223		[2]
$Tb_3Ni_2Ge_3$[d,e]	0.42027(3)	1.03313(9)	1.41114(11)	0.61271	4.5	This work
$Ho_3Ni_2Ge_3$[a,f]	0.41745(1)	1.02423(2)	1.39915(3)	0.59823	2.8	This work
$Ho_3Ni_2Ge_3$	0.41694(4)	1.02487(9)	1.39977(10)	0.59813		[2]

[a] - Crystallographic data used with permission of JCPDS – International Centre for Diffraction Data.
[b] - Atomic positions of $Sm_3Co_2Ge_3$: Sm1 8*f* [0, 0.4182(2), 0.1112(2)], Sm2 4*c* [0, 0.1346(2), 1/4], Co 8*f* [0, 0.7124(4), 0.0898(4)], Ge1 4*c* [0, 0.8302(5), 1/4], Ge2 8*f* [0, 0.1212(4), 0.0452(3)]. atomic displacement parameters of all atoms β_{11}=0.014048, β_{22}=0.002184, β_{33}=0.001242 ($\beta_{11}=B_{11}/[2a]^2$, $\beta_{22}=B_{11}/[2b]^2$, $\beta_{33}=B_{33}/[2c]^2$).
[c] - Atomic positions of $Er_3Co_2Ge_3$: Er1 8*f* [0, 0.4260(2), 0.1156(2)]; Er2 4*c* [0, 0.1398(3), 1/4]; Co 8*f* [0, 0.7200(5), 0.1011(4)]; Ge1 4*c* [0, 0.8420(5), 1/4]; Ge2 8*f* [0, 0.1240(4), 0.0416(3)], atomic displacement parameters of all atoms β_{11}=0.014501, β_{22}=0.002330, β_{33}=0.001312 ($\beta_{11}=B_{11}/[2a]^2$, $\beta_{22}=B_{11}/[2b]^2$, $\beta_{33}=B_{33}/[2c]^2$).
[d] - Atomic positions of $Tb_3Ni_2Ge_3$: Tb1 8*f* [0, 0.4109(4), 0.1106(3)]; Tb2 4*c* [0, 0.1342(6), 1/4]; Ni 8*f* [0, 0.6982(9), 0.1024(8)]; Ge1 4*c* [0, 0.8333(6), 1/4]; Ge2 8*f* [0, 0.1263(6), 0.0375(5)], atomic displacement parameters of all atoms β_{11}=0.014154, β_{22}=0.002342, β_{33}=0.001255 ($\beta_{11}=B_{11}/[2a]^2$, $\beta_{22}=B_{11}/[2b]^2$, $\beta_{33}=B_{33}/[2c]^2$).
[e] - Sample used for neutron diffraction study: sample contains 73 wt% of $Hf_3Ni_2Si_3$-type $Tb_3Ni_2Ge_3$, 20 wt% of TiNiSi-type TbNiGe [3,4] and 7 wt% of CrB-type TbGe [3,4].
[f] - Atomic positions of $Ho_3Ni_2Ge_3$: Ho1 8*f* [0, 0.4088(1), 0.1097(1)]; Ho2 4*c* [0, 0.1304(2), 1/4]; Ni 8*f* [0, 0.6941(5), 0.1012(4)]; Ge1 4*c* [0, 0.8381(4), 1/4]; Ge2 8*f* [0, 0.1209(3), 0.0364(3)], atomic displacement parameters of all atoms β_{11}=0.014346, β_{22}=0.002383, β_{33}=0.001277 ($\beta_{11}=B_{11}/[2a]^2$, $\beta_{22}=B_{11}/[2b]^2$, $\beta_{33}=B_{33}/[2c]^2$).

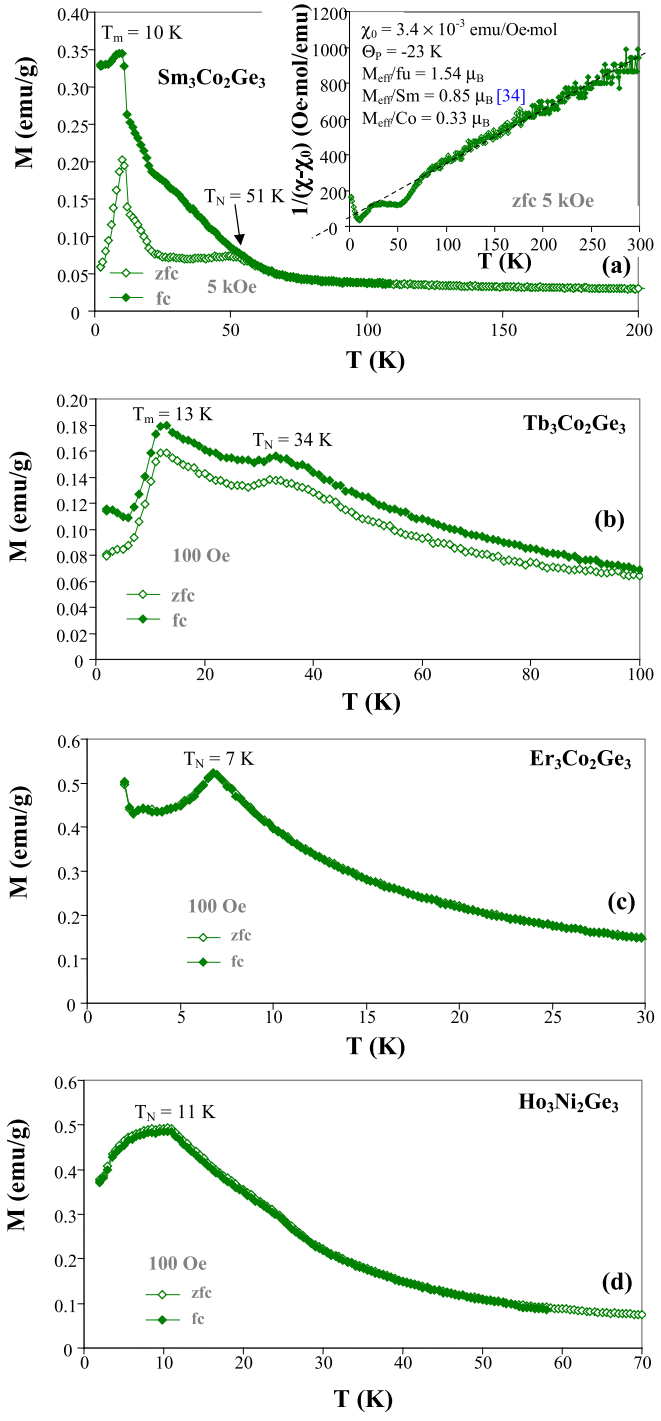

Fig. 1. Magnetization as a function of temperature of (a) $Sm_3Co_2Ge_3$, (b) $Tb_3Co_2Ge_3$, (c) $Er_3Co_2Ge_3$ and (d) $Ho_3Ni_2Ge_3$ (Insets in (a): modified Curie-Weiss fit to the inverse paramagnetic susceptibility).

Curie-Weiss law in the temperature range of ~90–300 K with a paramagnetic temperature Θ_P=−23 K and χ_0=3.4×10^{-3} emu/Oe mol, whereas paramagnetic susceptibilities of $Tb_3Co_2Ge_3$, $Er_3Co_2Ge_3$ and $Ho_3Ni_2Ge_3$ obey the Curie-Weiss law in the range of ca. 90–300 K (Insets in Fig. 2). The fit yields Weiss temperatures (Θ_P) of 8.6 K for $Tb_3Co_2Ge_3$, 4.6 K for $Er_3Co_2Ge_3$ and 2.5 K for $Ho_3Ni_2Ge_3$, suggesting weak overall magnetic interactions. Effective paramagnetic moments per formula unit (M_{eff}/fu) derived for $Sm_3Co_2Ge_3$, $Tb_3Co_2Ge_3$, $Er_3Co_2Ge_3$ and $Ho_3Ni_2Ge_3$ are 1.54 μ_B, 17.2 μ_B, 16.7 μ_B and 18.4 μ_B, respectively. These values yield effective paramagnetic moments per transition metal atom (M_{eff}/T) of 0.33 μ_B, 2.4 μ_B, 1.4 μ_B and 0.73 μ_B,

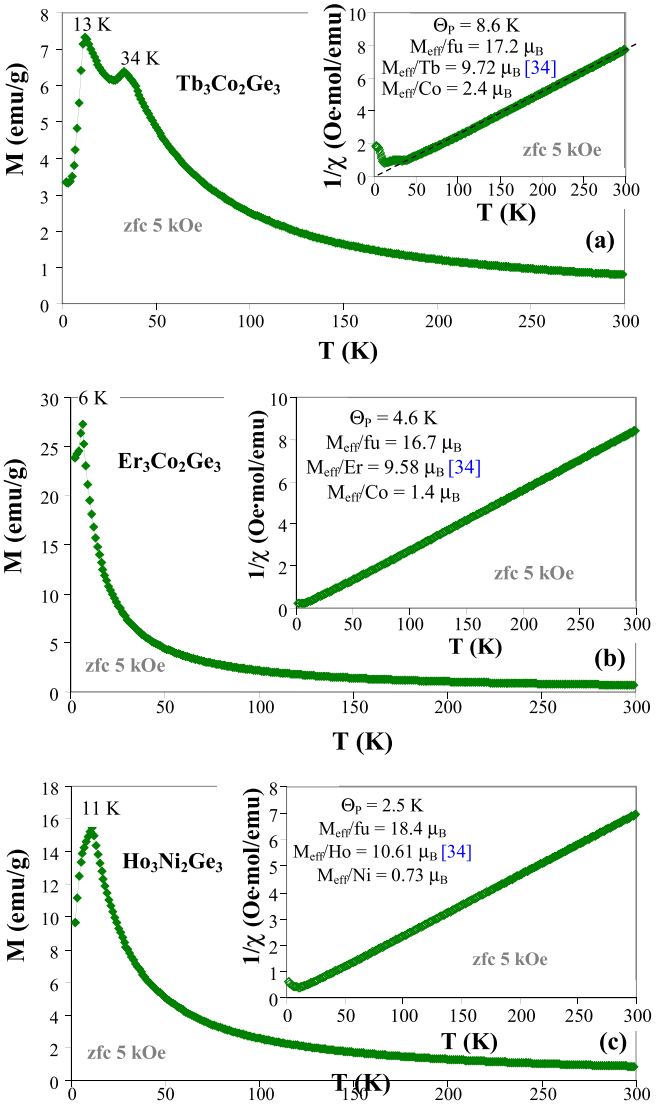

Fig. 2. Magnetization as a function of temperature in field of 5 kOe of (a) $Tb_3Co_2Ge_3$, (b) $Er_3Co_2Ge_3$ and (c) $Ho_3Ni_2Ge_3$ (Insets in Figures: Curie-Weiss fit to the inverse paramagnetic susceptibility).

respectively, if Sm, Tb, Ho and Er are assumed to have theoretical moments of 0.85 μ_B, 9.72 μ_B, 10.61 μ_B and 9.58 μ_B [34].

The magnetization vs field isotherms recorded at 2 K exhibit metamagnetic transitions with a critical field (H_{crit}) of ~5 kOe for $Sm_3Co_2Ge_3$, 20 kOe for $Tb_3Co_2Ge_3$, 4 kOe for $Er_3Co_2Ge_3$ and ~7 kOe for $Ho_3Ni_2Ge_3$ (Fig. 3). Above the metamagnetic transition field, the magnetization curves of $Tb_3Co_2Ge_3$, $Er_3Co_2Ge_3$ and $Ho_3Ni_2Ge_3$ show a saturation behaviour with the magnetization value of 6.5 μ_B, 7.0 μ_B and 8.0 μ_B per rare-earth atom in the field of 140 kOe ($M_{140\ kOe}/R$), whereas the magnetization per rare-earth atom (M_∞/R) by extrapolating to 1/H→0 is 8.0 μ_B for $Tb_3Co_2Ge_3$, 8.8 μ_B for $Er_3Co_2Ge_3$ and 9.5 μ_B for $Ho_3Ni_2Ge_3$ (theoretical terbium, holmium and erbium magnetic moments are 9 μ_B, 10 μ_B and 9 μ_B [34], respectively). This suggests an almost collinear field induced ferromagnetic state for Tb, Ho and Er sublattices in these compounds. The $Tb_3Co_2Ge_3$, $Er_3Co_2Ge_3$ and $Ho_3Ni_2Ge_3$ display negligible hysteresis, whereas magnetization of $Sm_3Co_2Ge_3$ exhibits an antiferromagnetic-like behaviour with hysteresis: residual magnetization per Sm (M_{res}/R) of 0.01 μ_B and coercive field (H_{coer}) of 13 kOe. The magnetization of $Sm_3Co_2Ge_3$ reaches the value of 0.21 μ_B ($M_{140\ kOe}$/Sm=0.7 μ_B) and formally for 1/H→0 M_∞/Sm extrapolates to 0.17 μ_B, which is less than the theoretical Sm magnetic moment of 0.71 μ_B [34].

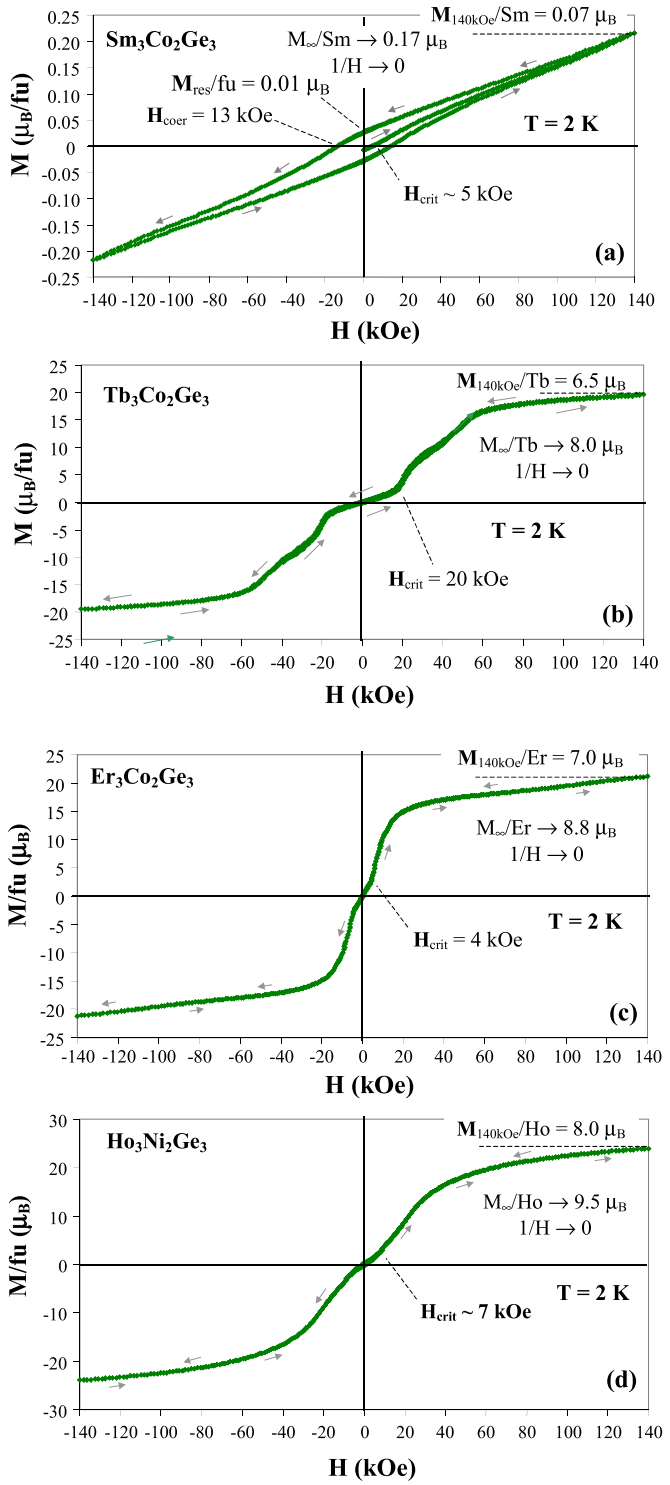

Fig. 3. Magnetization vs. magnetic field of (a) $Sm_3Co_2Ge_3$, (b) $Tb_3Co_2Ge_3$, (c) $Er_3Co_2Ge_3$ and (d) $Ho_3Ni_2Ge_3$ at 2 K in fields up to 140 kOe.

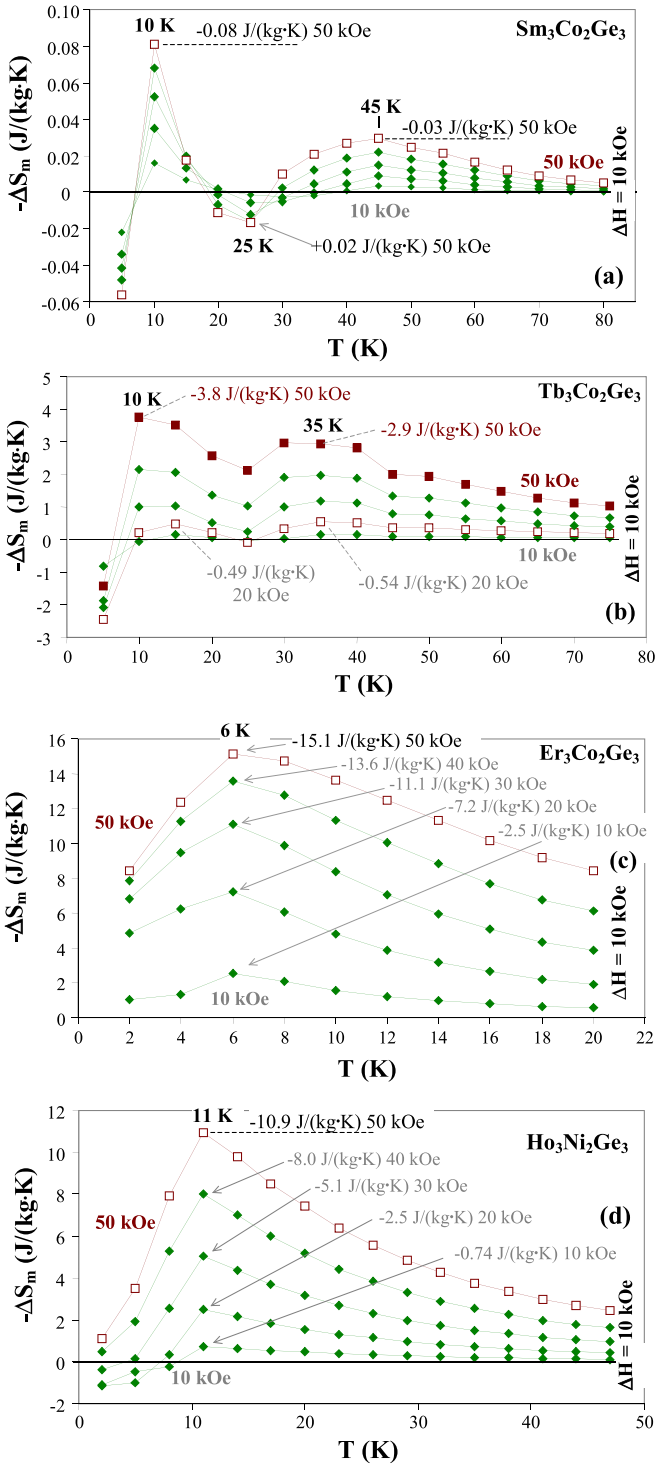

Fig. 4. Isothermal magnetic entropy change, $-\Delta S_m$, of (a) $Sm_3Co_2Ge_3$, (b) $Tb_3Co_2Ge_3$, (c) $Er_3Co_2Ge_3$ and (d) $Ho_3Ni_2Ge_3$ for a field change of 0–50 kOe.

The isothermal magnetic entropy change (ΔS_m) in $Sm_3Co_2Ge_3$, $Tb_3Co_2Ge_3$, $Er_3Co_2Ge_3$ and $Ho_3Ni_2Ge_3$ is calculated from the magnetization vs. magnetic field isotherms obtained near the magnetic transitions (Fig. 2s) using the Maxwell's thermodynamic relation [27]. The ΔS_m reaches values of −0.03 J/kg K at 45 K, +0.02 J/kg K at 25 K and −0.08 J/kg K at 10 K for $Sm_3Co_2Ge_3$ for a field change of 0–50 kOe (Fig. 4a). The ΔS_m reaches the maximum values of −2.9 J/kg K at 35 K and −3.8 J/kg K at 10 K for $Tb_3Co_2Ge_3$, −15.1 J/kg K at 6 K for $Er_3Co_2Ge_3$ and −10.9 J/kg K at 11 K for $Ho_3Ni_2Ge_3$ for a field change of 0–50 kOe (Fig. 4b–d).

For a field change of 0–140 kOe, the magnetic entropy change (ΔS_m) is −0.13 J/kg K at 40 K and −0.09 J/kg K at 10 K for $Sm_3Co_2Ge_3$ and −26.4 J/kg K at 14 K for $Ho_3Ni_2Ge_3$, whereas the applied magnetic field suppresses the entropy change around 6 K for $Er_3Co_2Ge_3$ (Fig. 5).

The maximum entropy change (ΔS_m^{max}) of the corresponding magnetic transitions vs. field change (ΔH) exhibits a non-linear dependence for all compounds, which corresponds to metamagnetic-type transitions. The ΔS_m^{max} indicates incomplete metamagnetic transitions for $Tb_3Co_2Ge_3$ at 35 K and 15 K in the fields of up to

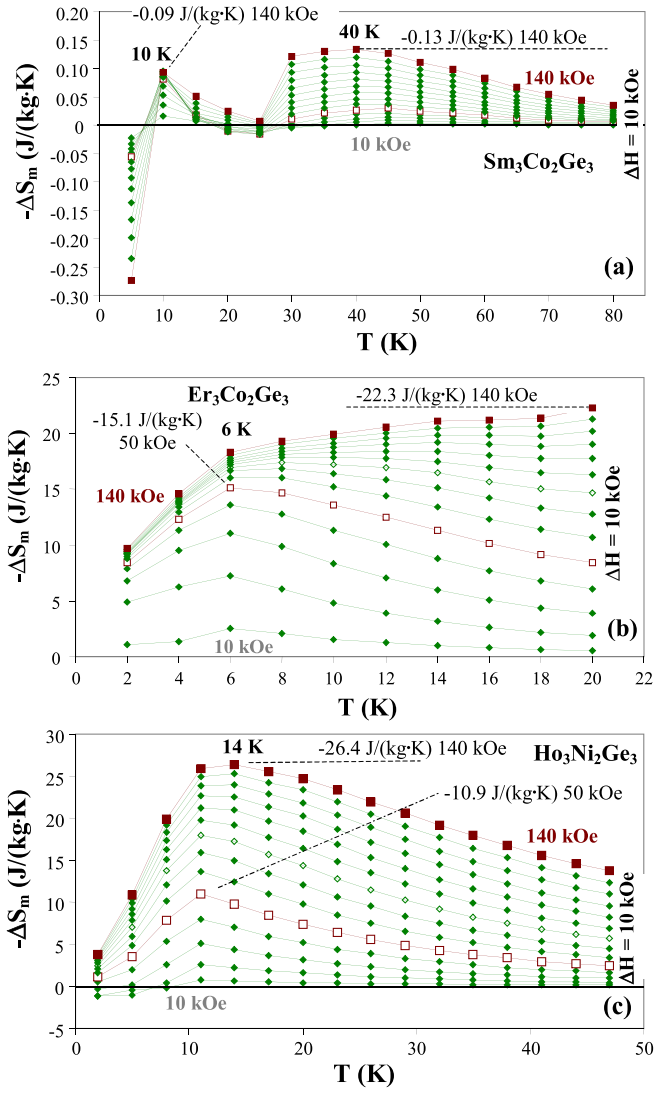

Fig. 5. Isothermal magnetic entropy change, $-\Delta S_m$, of (a) $Sm_3Co_2Ge_3$, (b) $Er_3Co_2Ge_3$ and (c) $Ho_3Ni_2Ge_3$ for a field change of 0–140 kOe.

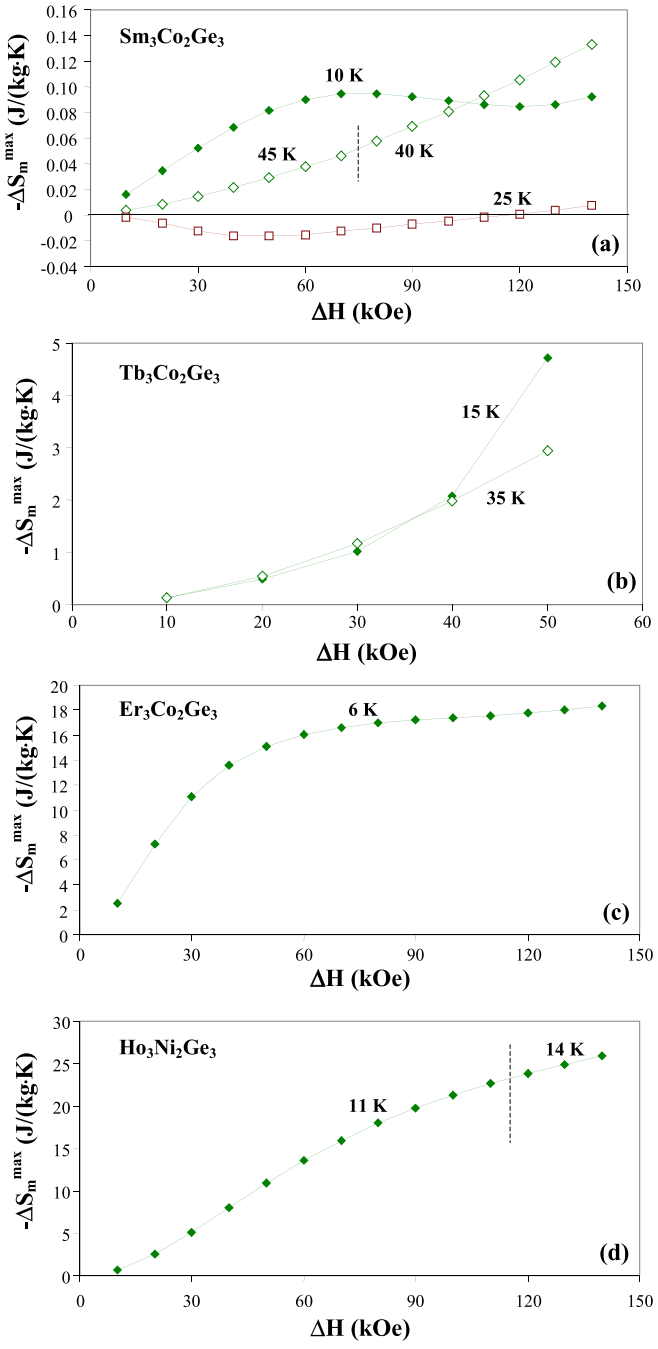

Fig. 6. The magnetic entropy change of corresponding magnetic transitions ($-\Delta S_m^{max}$) vs. field change (ΔH) of (a) $Sm_3Co_2Ge_3$, (b) $Tb_3Co_2Ge_3$, (c) $Er_3Co_2Ge_3$ and (d) $Ho_3Ni_2Ge_3$.

50 kOe. Also the ΔS_m^{max} indicates incomplete metamagnetic transitions for $Sm_3Co_2Ge_3$ at 45 K (40 K) and $Ho_3Ni_2Ge_3$ at 11 K (14 K) in the field of up to 140 kOe, whereas the ΔS_m^{max} shows complete metamagnetic transitions for $Sm_3Co_2Ge_3$ at 25 K and 10 K in field of ~70 kOe and it exhibits a complete metamagnetic transition for $Er_3Co_2Ge_3$ at 6 K around 60 kOe (Fig. 6).

The results of the magnetic measurements are summarized in Table 2.

3.3. Neutron diffraction study

The '$Tb_3Ni_2Ge_3$' sample contains the TiNiSi-type TbNiGe and CrB-type TbGe impurities [3,4] with known magnetic ordering: TbNiGe shows an *a*-axis antiferromagnetic ordering at T_N=18 K with a **K**=[0.716, 0.309, 0] propagation vector [35], whereas TbGe exhibits a *c*-axis antiferromagnetic ordering with a **K**=[0, 0, 1/2] propagation vector below T_N=60 K with a subsequent transformation in to a *b*-axis antiferromagnet with a **K'**=[1/2, 0, 1/2] vector between 33 K and 20 K [36]. These data permit to determine the magnetic ordering of the $Tb_3Ni_2Ge_3$ compound. Since the magnetic moment of the Ni sublattice (M_{Ni}^{theory}=0.616 μ_B [34]) is negligible in comparison with the terbium magnetic moment (M_{Tb}^{theory}=9 μ_B [34]), models with a magnetic ordering of the Ni sublattice were not considered in the present refinement. Also, this assumption is based on the fact that many rare-earth-rich binary *R*-Ni or ternary *R*-Ni-Ge compounds have been reported to have no ordered Ni magnetic moments due to either *R*→Ni electron transfer or Ni-Ge electronic hybridization [37,38].

$Tb_3Ni_2Ge_3$ is a paramagnet down to 40 K, whereas at 20 K the observed set of magnetic reflections reveals a commensurate magnetic ordering of $Tb_3Ni_2Ge_3$ with a $\mathbf{K}_0$=[0, 0, 0] propagation vector. The set of additional reflections with $\mathbf{K}_1$=[0, 0, ± 1/3] indicates a low-temperature transformation of the $Tb_3Ni_2Ge_3$ magnetic ordering at T_m^{ND}=15 K and down to 1.5 K (Fig. 7). The structural and magnetic reflections of TbNiGe and TbGe are shown in Fig. 7, whereas small unindexed reflections (that are marked in Fig. 7c) may belong to unidentified impurity phases.

Thermal evolution of the strongest magnetic reflections indicates

Table 2
Magnetic properties of $Hf_3Ni_2Si_3$-type {Sm, Tb, Er}$_3Co_2Ge_3$ and {Tb, Ho}$_3Ni_2Ge_3$ compounds: effective magnetic moment per formula (M_{eff}/fu) and per transition metal atom (M_{eff}/T), respectively, paramagnetic Weiss temperature (Θ_P), Néel point (T_N), temperature of low-temperature transition (T_m), magnetization per rare earth atom in field of 140 kOe at 2 K ($M_{140\ kOe}/R$), residual magnetization per rare earth atom (M_{res}/R), coercive field (H_{coer}) and critical field (H_{crit}) at 2 K. The magnetocaloric effect (MCE) is given in terms of isothermal magnetic entropy change (ΔS_m) in field change of 0–50 kOe and 0–140 kOe at corresponding temperature.

Compound	M_{eff}/fu (μ_B)	M_{eff}/T (μ_B)	Θ_P (K)	T_N (K)	T_m (K)	$M_{140\ kOe}/R$ (μ_B)	M_{res}/R (μ_B)	H_{coer} (kOe)	H_{crit} (kOe)	ΔS_m (J/kg·K) 0–50 kOe	ΔS_m (J/kg·K)0–140 kOe	Refs.
$Sm_3Co_2Ge_3$[a]	1.54	0.33	−23	51	10	0.07	0.01	13	~5	−0.03 (45 K) +0.02 (25 K) −0.08 (10 K)	−0.13 (40 K) – −0.09 (10 K)	[b]
$Sm_3Co_2Ge_3$	4.14		−270	60	10							[1]
$Tb_3Co_2Ge_3$	17.2	2.4	8.6	34[e]	13[d]	6.5	–	–	20	−2.9 (35 K) −3.8 (10 K)		[b]
$Tb_3Co_2Ge_3$	15.46		−3.4	> 10								[1]
$Er_3Co_2Ge_3$	16.7	1.4	4.6	7	–	7.0	–	–	4	−15.1 (6 K)	−22.3 (20 K)	[b]
$Er_3Co_2Ge_3$	15.66		3.8	< 10								[1]
$Tb_3Ni_2Ge_3$				33[e]	15[f]							[b]
$Ho_3Ni_2Ge_3$	18.4	0.73	2.5	11	–	8.0	–	–	7	−10.9 (11 K)	−26.4 (14 K)	[b]
$Ho_3Ni_2Ge_3$	18.60		−2.9	7								[2]

[a] - Paramagnetic susceptibility of $Sm_3Co_2Ge_3$ leads to modified Curie-Weiss law with $\chi_0=3.4\times10^{-3}$ emu/Oe mol.
[b] - This work.
[e] - High-temperature antiferromagnetic ordering of $Tb_3Co_2Ge_3$: $(\mathbf{AF}_a+\mathbf{AF}_b+\mathbf{AF}_c)^{\mathbf{K0}}$ (***Pmm'c'***)$+\mathbf{AF}_{flat\ spiral}{}^{\mathbf{K1}}$ ($\mathbf{K}_0$=[0, 0, 0], $\mathbf{K}_1$=[± 1/3, 0, 0], ***Pmm'c'***={**1**, $\mathbf{2}_x$}×{**1**, $\mathbf{m}_x$/[1/2, 1/2, 0]} ×{**1**, $\mathbf{2}_y$'/[0, 0, 1/2]} [1].
[d] - Low-temperature antiferromagnetic ordering of $Tb_3Co_2Ge_3$: $(\mathbf{AF}_a+\mathbf{AF}_b+\mathbf{AF}_c)^{\mathbf{K0}}$ (***Pmm'c'***)$+\mathbf{AF}_{flat\ spiral}{}^{\mathbf{K1}}+\mathbf{AF}_a{}^{\mathbf{K2}}$ ($\mathbf{K}_0$=[0, 0, 0], $\mathbf{K}_1$=[± 1/3, 0, 0]; $\mathbf{K}_2$=[1/2, 0, 0]) [1].
[e] - High-temperature antiferromagnetic ordering of $Tb_3Ni_2Ge_3$: $(\mathbf{AF}_a+\mathbf{AF}_c)^{\mathbf{K0}}$ (***C2'/c***), $\mathbf{K}_0$=[0, 0, 0], ***C2'/c***={**1**, $\mathbf{2}_y$'/[0 0 1/2]} ×{**1**, $\mathbf{m}_y$/[0 0 1/2]}×{**1**, **1'**/[1/2 1/2 0]}.
[f] - Low-temperature antiferromagnetic ordering of $Tb_3Ni_2Ge_3$: $(\mathbf{AF}_a+\mathbf{AF}_c)^{\mathbf{K0}}$ (***C2'/c***)$+\mathbf{AF}_a{}^{\mathbf{K1}}$, $\mathbf{K}_0$=[0, 0, 0], $\mathbf{K}_1$=[0, 0, ± 1/3].

the Néel point of $Tb_3Ni_2Ge_3$ above 20 K, whereas magnetization as a function of temperature of the 'Tb$_3$Ni$_2$Ge$_3$' sample shows an antiferromagnetic transition of $Tb_3Ni_2Ge_3$ at T_N=33 K (the antiferromagnetic transition of 7 wt% TbGe vanishes in the field of 5 kOe and the transition at 19 K belongs to the 20 wt% of TbNiGe) (Figs. 8a and b).

The terbium sublattice of the $Tb_3Ni_2Ge_3$ compound (space group *Cmcm*) consists of the Tb1 8*f* and Tb2 4*c* sublattices (the coordinates for the 4*c* and 8*f* sites and symmetry operators for the corresponding terbium atom are given in Table 3). Magnetic space groups [29–31] were used for the analysis of the neutron diffraction data. The commensurate magnetic reflections correspond to the *ac*-antiferromagnetic ordering of $Tb_3Ni_2Ge_3$ with the ***C2'/c*** (N 15.3.94) [31] magnetic space group and the $\mathbf{K}_0$=[0, 0, 0] vector. The incommensurate reflections correspond to the *a*-axis sine modulated antiferromagnetic ordering with the $\mathbf{K}_1$=[0, 0, ± 1/3] vector. Thus, below T_N=33 K and down to $T_m{}^{ND}$=15 K $Tb_3Ni_2Ge_3$ is an *ac*-antiferromagnet $(\mathbf{AF}_a+\mathbf{AF}_c)^{\mathbf{K0}}$ (***C2'/c***) with the ***C2'/c*** magnetic space group, $\mathbf{K}_0$ vector and $a_{Tb3Ni2Ge3}\times b_{Tb3Ni2Ge3}\times c_{Tb3Ni2Ge3}$ magnetic unit cell, whereas below $T_m{}^{ND}$=15 K, its magnetic structure is a sum of the $(\mathbf{AF}_a+\mathbf{AF}_c)^{\mathbf{K0}}$ (***C2'/c***) and $\mathbf{AF}_a{}^{\mathbf{K1}}$ magnetic components ($\mathbf{AF}_a{}^{\mathbf{K1}}$ the sine modulated *a*-antiferromagnet with $\mathbf{K}_1$ vector) with a magnetic unit cell $a_{Tb3Ni2Ge3}\times b_{Tb3Ni2Ge3}\times 3c_{Tb3Ni2Ge3}$.

The resulting magnetic moment of the Tb1 and Tb2 atoms: $\mathbf{M}_{Tbji}=\mathbf{i}\cdot[M_{a Tbji}{}^{\mathbf{K0}}+ M_{a Tbji}{}^{\mathbf{K1}}\cdot\cos(2\pi n/3+\phi_{ji})]+\mathbf{k}\cdot M_{c Tbji}{}^{\mathbf{K0}}$, where n=0...1, 2... and is the number of the unit cell along the *a* axis of $Tb_3Ni_2Ge_3$; **i** and **k** are the orthonormal vectors (**i** coincides with the *a* axis and **k** with the *c* axis); magnetic moment $M_{a Tbji}{}^{\mathbf{K0}}$ and $M_{c Tbji}{}^{\mathbf{K0}}$ are along *a* and *c* axis, respectively, with a propagation vector $\mathbf{K}_0$=[0, 0, 0]; $M_{a Tbji}{}^{\mathbf{K1}}$ is an amplitude of the magnetic moment and $\phi_{ji}{}^{K1}$ is a phase angle (propagation vector $\mathbf{K}_1$=[0, 0, ± 1/3]. The magnetic components are listed in Table 4. The magnitude of the Tb1 and Tb2 moments reaches values of 8.6 μ_B and 9.2 μ_B, respectively, at 1.5 K, which corresponds fairly well to the theoretical Tb magnetic moment of 9 μ_B [34].

The terbium sublattice is set of the 'Tb2-2Tb1' clusters connected via 'Tb1-Tb1' pairs with Tb2-Tb1 and Tb1-Tb1 distances of 0.3470 nm and 0.3624 nm, respectively (the distances are given at room temperature). The magnetic structure of $Tb_3Ni_2Ge_3$ is the set of these 'Tb2-2Tb1' clusters ('Tb2^1-Tb1^1, Tb1^4', 'Tb2^2-Tb1^2, Tb1^3', 'Tb2^3-Tb1^5, Tb1^8' and 'Tb2^4-Tb1^6, Tb1^7') with antiferromagnetically ordered magnetic moments of the Tb2 and Tb1 atoms for low-temperature and high-temperature magnetic components. The magnetic moments of 'Tb1^1-Tb1^3', 'Tb1^2-Tb1^4', 'Tb1^5-Tb1^7' and 'Tb1^6-Tb1^8' pairs with the shortest distances in the Tb1 sublattice are ferromagnetically ordered (Fig. 9). The Tb2 4*c* sublattice plays a dominant role in the high-temperature magnetic ordering of $Tb_3Ni_2Ge_3$ as in $Tb_3Co_2Ge_3$ [1]: the magnetic moment of the Tb2 atoms is larger than the magnetic moment of the Tb1 atoms down to 1.5 K ($M_{Tb2i} > M_{Tb1i}$) (see Table 4 and Fig. 8a).

4. Discussion

Rare-earth clusters 'Tb2-2Tb1' of the rare-earth sublattice containing Tb1 *8f* (symmetry of site *Pm*={**1**, $\mathbf{m}_x$}) and Tb2 *4c* (symmetry of site *Pmc*2_1={**1**, $\mathbf{m}_x$}×{**1**, $\mathbf{2}_y$/[0, 0, 1/2]}) are attributes of the $Hf_3Ni_2Si_3$-type lattice and they determine the magnetic ordering of $Tb_3Co_2Ge_3$ [1] and $Tb_3Ni_2Ge_3$, meanwhile the sublattice with a higher symmetry (Tb2) plays a dominant role in magnetic ordering of $Tb_3Ni_2Ge_3$ and $Tb_3Co_2Ge_3$. A minor distortion of the unit cell from $Tb_3Co_2Ge_3$ to $Tb_3Ni_2Ge_3$ (expansion of the unit cell in the *ac*-plane, supression along the *b* axis and shifting of the 'Tb2-2Tb1' clusters) leads to the following changes in the magnetic structure (see Table 2):

– supression of the *b*-axis antiferromagnetic component in $Tb_3Ni_2Ge_3$;

– ferromagnetically ($Tb_3Co_2Ge_3$) and antiferromagnetically ($Tb_3Ni_2Ge_3$) ordered Tb1 and Tb2 magnetic moments in the 'Tb2-2Tb1' cluster;

– a low-temperature magnetic unit cell of $Tb_3Co_2Ge_3$ ($6a_{Tb3Co2Ge3}\times b_{Tb3Co2Ge3}\times c_{Tb3Co2Ge3}$) is transformed into $a_{Tb3Ni2Ge3}\times b_{Tb3Ni2Ge3}\times 3c_{Tb3Ni2Ge3}$ of $Tb_3Ni_2Ge_3$;

– magnetic space groups of the $\mathbf{K}_0$ vector are ***Pmm'c'*** for $Tb_3Co_2Ge_3$ and ***C2'/c*** for $Tb_3Ni_2Ge_3$ (due to different antiferromagnetic ordering of the 'Tb2-2Tb1' clusters).

Meanwhile, both $Tb_3Ni_2Ge_3$ and $Tb_3Co_2Ge_3$ exhibit a similar high-temperature *ac*-plane (or dominant *ac*-plane) antiferromagnetic ordering and a low-temperature ordering with an additional *a*-axis antiferromagnetic component. Similar antiferromagnetic ordering is suggested in the $Hf_3Ni_2Si_3$-type rare-earth germanides with different magnetic space groups and propagation vectors, whereas the

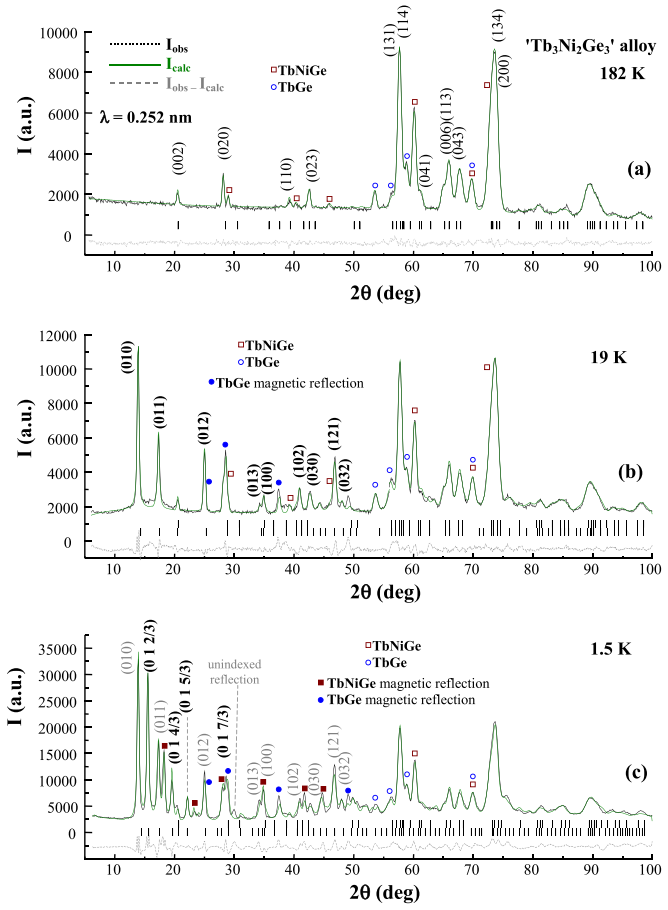

Fig. 7. Neutron diffraction patterns of '$Tb_3Ni_2Ge_3$' sample (a) at 182 K (paramagnetic state of $Tb_3Ni_2Ge_3$), (b) at 19 K (*ac*-antiferromagnetic ordering of $Tb_3Ni_2Ge_3$: $(\mathbf{AF}_a+\mathbf{AF}_c)^{\mathbf{K0}}$ $(\boldsymbol{C2'/c})$ with $\mathbf{K}_0$=[0, 0, 0] vector and (c) at 1.5 K (*ac*-antiferromagnetic ordering of $Tb_3Ni_2Ge_3$: $(\mathbf{AF}_a+\mathbf{AF}_c)^{\mathbf{K0}}$ $(\boldsymbol{C2'/c})+\mathbf{AF}_a^{\mathbf{K1}}$ with $\mathbf{K}_0$=[0, 0, 0] and $\mathbf{K}_1$=[0, 0, ± 1/3] vectors). The first row of ticks refers to the nuclear Bragg peaks whereas the second row of lines refers to the magnetic reflections of $Tb_3Ni_2Ge_3$. The (*hkl*) indices of the strongest magnetic reflections of $Tb_3Ni_2Ge_3$ are indicated in Figs. 7b and 7c. The strongest structural and magnetic reflections of the TbNiGe and TbGe impurities are marked in Figures.

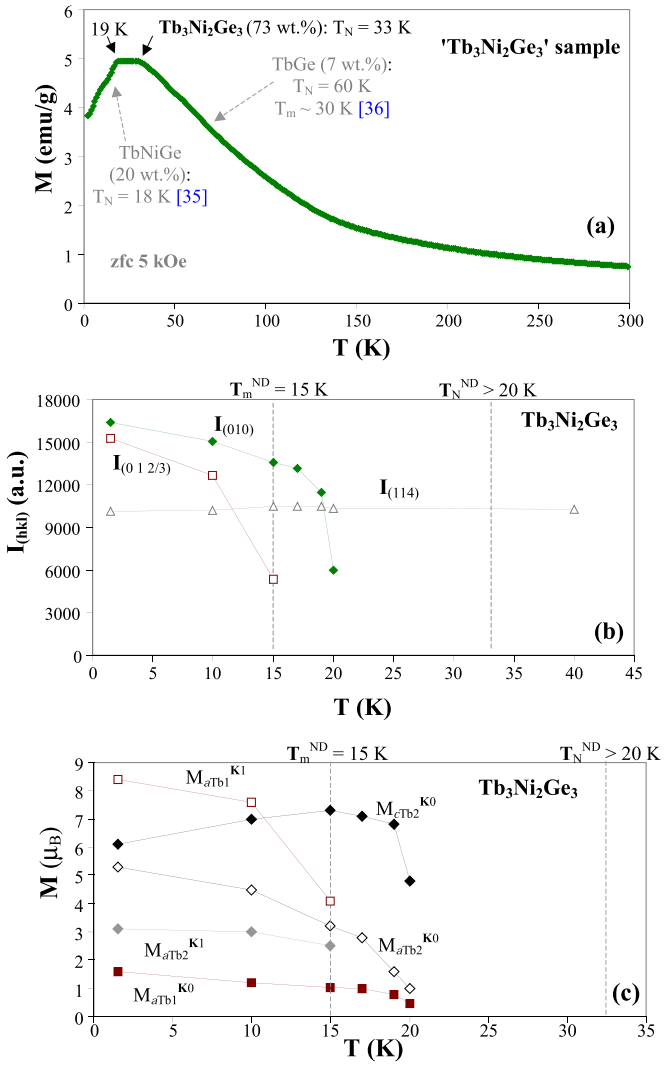

Fig. 8. (a) Magnetization as a function of temperature of '$Tb_3Ni_2Ge_3$' sample; (b) thermal evolution of the strongest magnetic reflections $I_{(hkl)}$ in the neutron diffraction patterns of $Tb_3Ni_2Ge_3$; and (c) $M_{aTb1,2}{}^{\mathbf{K0}}$, $M_{cTb1,2}{}^{\mathbf{K0}}$ the magnetic moments and $M_{aTb1,2}{}^{\mathbf{K1}}$, $M_{cTb1,2}{}^{\mathbf{K1}}$ the amplitude of magnetic moments of Tb1 and Tb2 atoms with the $\mathbf{K}_0$=[0, 0, 0] and $\mathbf{K}_1$=[0, 0, ± 1/3] propagation vectors.

Table 3
Coordinates of the *8f* and *4c* sites in the *Cmcm* [a] space group (retained by $Tb_3Ni_2Ge_3$) and the corresponding symmetry operators for the crystal and magnetic lattices.

N	x/*a*	y/*b*	z/*c*	Symmetry operator of crystal lattice	$M_{aTbj}{}^{K0}$	$M_{bTbj}{}^{K0}$	$M_{cTbj}{}^{K0}$	Symmetry operator of magnetic lattice[b]
$Tb1^1$	0	$+y_{Tb1}$	$+z_{Tb1}$	**1**, $\mathbf{m}_x$	0	0	+	**1**
$Tb1^2$	0	$-y_{Tb1}$	$1/2+z_{Tb1}$	$\mathbf{m}_y$/[0, 0, 1/2], $\mathbf{2}_z$/[0, 0, 1/2]	0	0	+	$\mathbf{m}_y$/[0, 0, 1/2]
$Tb1^3$	0	$-y_{Tb1}$	$-z_{Tb1}$	**i**, $\mathbf{2}_x$	0	0	+	**i′**
$Tb1^4$	0	$+y_{Tb1}$	$1/2-z_{Tb1}$	$\mathbf{2}_y$/[0, 0, 1/2], $\mathbf{m}_z$/[0, 0, 1/2]	0	0	+	$\mathbf{2}_y$′/[0 0 1/2]
$Tb1^5$	1/2	$1/2+y_{Tb1}$	$+z_{Tb1}$	**1**/[1/2, 1/2, 0], $\mathbf{m}_x$/[1/2, 1/2, 0]	0	0	–	**1**′/[1/2, 1/2, 0]
$Tb1^6$	1/2	$1/2-y_{Tb1}$	$1/2+z_{Tb1}$	$\mathbf{m}_y$/[1/2, 1/2, 1/2], $\mathbf{2}_z$/[1/2, 1/2, 1/2]	0	0	–	$\mathbf{m}_y$′/[1/2 1/2 1/2]
$Tb1^7$	1/2	$1/2-y_{Tb1}$	$-z_{Tb1}$	**i**/[1/2, 1/2, 0], $\mathbf{2}_x$/[1/2, 1/2, 0]	0	0	–	**i**/[1/2 1/2 0]
$Tb1^8$	1/2	$1/2+y_{Tb1}$	$1/2-z_{Tb1}$	$\mathbf{2}_y$/[1/2, 1/2, 1/2], $\mathbf{m}_z$/[1/2, 1/2, 1/2]	0	0	–	$\mathbf{2}_y$/[1/2, 1/2, 1/2]
$Tb2^1$	0	$+y_{Tb2}$	1/4	**1**, $\mathbf{m}_x$, $\mathbf{2}_y$/[0, 0, 1/2], $\mathbf{m}_z$/[0, 0, 1/2]	+	0	+	**1**, $\mathbf{2}_y$′/[0 0 1/2]
$Tb2^2$	0	$-y_{Tb2}$	3/4	$\mathbf{m}_y$/[0, 0, 1/2], $\mathbf{2}_z$/[0, 0, 1/2], **i**, $\mathbf{2}_x$	+	0	+	$\mathbf{m}_y$/[0 0 1/2], **i′**
$Tb2^3$	1/2	$1/2 + y_{Tb2}$	1/4	**1**/[1/2, 1/2, 0], $\mathbf{m}_x$/[1/2, 1/2, 0], $\mathbf{2}_y$/[1/2, 1/2, 1/2], $\mathbf{m}_z$/[1/2, 1/2, 1/2]	–	0	–	**1′**/[1/2 1/2 0], $\mathbf{2}_y$/[1/2 1/2 1/2]
$Tb2^4$	1/2	$1/2 - y_{Tb2}$	3/4	$\mathbf{m}_y$/[1/2, 1/2, 1/2], $\mathbf{2}_z$/[1/2, 1/2, 1/2], **i**/[1/2, 1/2, 0], $\mathbf{2}_x$/[1/2, 1/2, 0]	–	0	–	**i**/[1/2 1/2 0] $\mathbf{m}_y$′/[1/2 1/2 1/2],

[a] - *Cmcm*={**1**, $\mathbf{m}_x$}×{**1**, $\mathbf{2}_y$/[0 0 1/2]}×{**1**, $\mathbf{m}_y$/[0, 0, 1/2]}×{**1**, **1**/[1/2 1/2 0]} and one of subgroup of *Cmcm* space group is *C*2/*c*={**1**, $\mathbf{2}_y$/[0 0 1/2]}×{**1**, $\mathbf{m}_y$/[0 0 1/2]}×{**1**, **1**/[1/2 1/2 0]}.

[b] - The set of symmetry operators corresponds to the magnetic space group N 15.3.94 $\boldsymbol{C2'/c}$={**1**, $\mathbf{2}_y$′/[0 0 1/2], **i′**, $\mathbf{m}_y$/[0 0 1/2], **1′**/[1/2 1/2 0], $\mathbf{2}_y$/[1/2 1/2 1/2], **i**/[1/2 1/2 0], $\mathbf{m}_y$′/[1/2 1/2 1/2]}={**1**, $\mathbf{2}_y$′/[0 0 1/2]} ×{**1**, $\mathbf{m}_y$/[0 0 1/2]}×{**1**, **1′**/[1/2 1/2 0]} [31].

Table 4
Crystallographic and magnetic parameters of the $Hf_3Ni_2Si_3$-type $Tb_3Ni_2Ge_3$ compound at different temperatures: cell parameters *a*, *b* and *c*, magnetic moment M_{aTbji}^{K0} and M_{cTbji}^{K0} along *a* and *c* axis, respectively (propagation vector $\mathbf{K}_0$=[0, 0, 0]), amplitude of magnetic moment M_{aTbji}^{K1} and ϕ_{ji}^{K1} phase angle (propagation vector $\mathbf{K}_1$=[0, 0, ± 1/3]) and magnitude (amplitude) of resulting magnetic moment $|\mathbf{M}_{Tbji}|$ of the corresponding Tbj^i atom [a]. R_F (crystal structure) and R_F^m (magnetic structure) are reliability factors of the Rietveld refinement.

T (K)	Cell parameters	R_F (%)	Atom	M_{aTbji}^{K0} (μ_B)	M_{cTbji}^{K0} (μ_B)	M_{aTbji}^{K1} (μ_B)	ϕ_{ji}^{K1} (rad)	$\|\mathbf{M}_{Tbji}\|$ (μ_B)	R_F^m (%)
Paramagnet down to T_N=33 K									
182	*a*=0.4191(1) nm	4.3							
	b=1.0318(2) nm								
	c=1.4054(3) nm								
ac-antiferromagnet below T_N=33 K of ***C2′/c*** magnetic space group with $\mathbf{K}_0$=[0, 0, 0] propagation vector: $(\mathbf{AF}_a+\mathbf{AF}_c)^{K0}$ (***C2′/c***)									
19	*a*=0.41837(8) nm	5.3	$Tb1^1$, $Tb1^2$, $Tb1^3$, $Tb1^4$	0	0.76(5)			0.76(5)	10.2
	b=1.0309(2) nm		$Tb1^5$, $Tb1^6$, $Tb1^7$, $Tb1^8$	0	−0.76(5)			0.76(5)	
	c=1.4025(3) nm		$Tb2^1$, $Tb2^2$	−1.6(2)	−6.8(1)			7.0(1)	
			$Tb2^3$, $Tb2^4$	1.6(2)	6.8(1)			7.0(1)	
ac-antiferromagnet at T_m=15 K and down to 1.5 K: sum of commensurate $(\mathbf{AF}_a+\mathbf{AF}_c)^{K0}$ (***C2′/c***) and *a*-axis sine modulated $\mathbf{AF}_a^{K1}$ ($\mathbf{K}_1$=[0, 0, ± 1/3]) magnetic components									
1.5	*a*=0.41827(11) nm	5.7	$Tb1^1$	0	1.6(1)	8.4(1)	0	8.6(1)	7.4
	b=1.0316(2) nm		$Tb1^2$	0	1.6(1)	8.4(1)	−2π/3	8.6(1)	
	c=1.4043(3) nm		$Tb1^3$	0	1.6(1)	8.4(1)	0	8.6(1)	
			$Tb1^4$	0	1.6(1)	8.4(1)	2π/3	8.6(1)	
			$Tb1^5$	0	−1.6(1)	8.4(1)	π	8.6(1)	
			$Tb1^6$	0	−1.6(1)	8.4(1)	π/3	8.6(1)	
			$Tb1^7$	0	−1.6(1)	8.4(1)	π	8.6(1)	
			$Tb1^8$	0	−1.6(1)	8.4(1)	−π/3	8.6(1)	
			$Tb2^1$	−5.3(1)	−6.1(2)	3.1(3)	0	9.2(2)	
			$Tb2^2$	−5.3(1)	−6.1(2)	3.1(3)	2π/3	9.2(2)	
			$Tb2^3$	5.3(1)	6.1(2)	3.1(3)	−π/3	9.2(2)	
			$Tb2^4$	5.3(1)	6.1(2)	3.1(3)	−π/3	9.2(2)	

[a] - Atomic positions of Tbj^i atoms are given in Table 3.

$Hf_3Ni_2Si_3$-type silicides may show a ferro-antiferromagnetic ordering due to supression (distortion) of the unit cell and corresponding transformation of the '*R*2-2*R*1' clusters. e.g. $Dy_3Co_2Si_3$ exhibits a ferromagnetic-type transition [39].

The magnetic entropy change (ΔS_m) indicates a field-induced transformation of the initial antiferromagnetic ordering in these compounds: a negative value of ΔS_m corresponds to the field-induced ferromagnetic ordering (metamagnetic transition) and a positive value of ΔS_m corresponds to the antiferromagnetic ordering. Thus, the magnetic entropy change vs. temperature shows transformation of the magnetic structure of the field sensitive $Sm_3Co_2Ge_3$, $Tb_3Co_2Ge_3$, $Er_3Co_2Ge_3$ and $Ho_3Ni_2Ge_3$ compounds by an indirect method. These data agree with the magnetization vs. temperature dependences (see Figs. 1 and 4) and neutron diffraction study of $Tb_3Co_2Ge_3$ in the zero-applied field [1]. The ΔS_m indicates a complex magnetic ordering of $Sm_3Co_2Ge_3$, two consecutive transformation of the magnetic structure

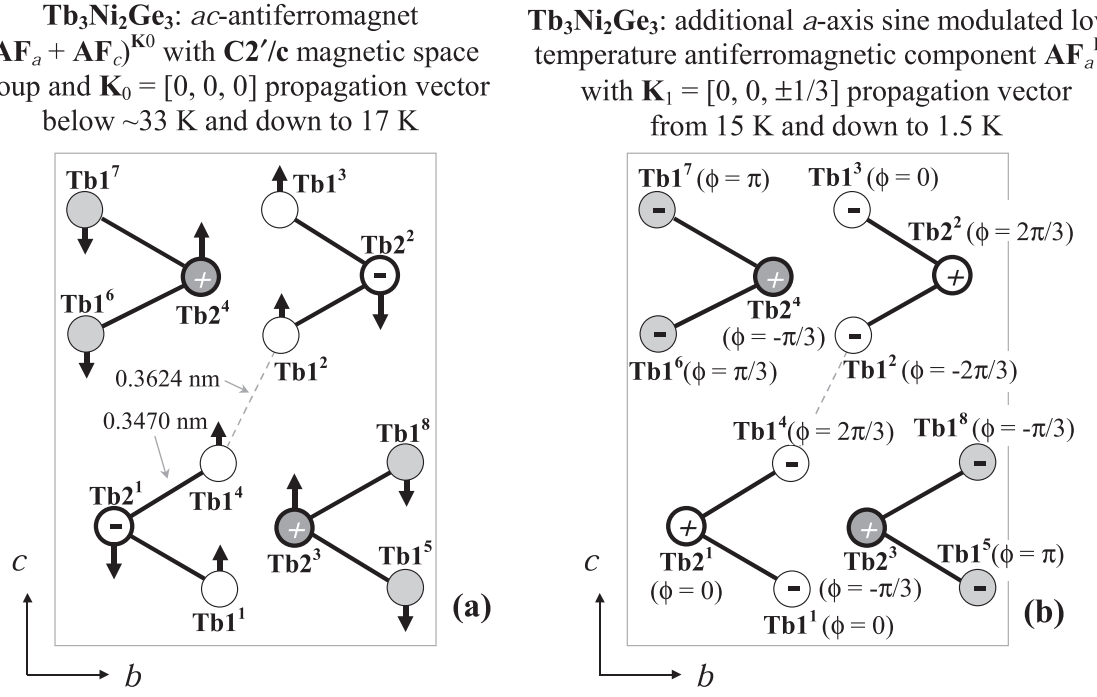

Fig. 9. (a) Magnetic structure of $Tb_3Ni_2Ge_3$ below ~33 K and down to 17 K and (b) additional low-temperature magnetic component in the $Tb_3Ni_2Ge_3$ magnetic structure (from 15 K and down to 1.5 K). The shortest Tb1-Tb1 and Tb1-Tb2 interatomic distances are shown in Figure.

of $Tb_3Co_2Ge_3$ and one transformation of the magnetic structure for $Er_3Co_2Ge_3$ and $Ho_3Ni_2Ge_3$.

In case of $Tb_3Co_2Ge_3$, $Er_3Co_2Ge_3$ and $Ho_3Ni_2Ge_3$, magnetic moment of the transition metal sublattice is negligible in comparison with the magnetic moment of the rare-earth sublattice. In meantime, the magnetic nature of $Sm_3Co_2Ge_3$ may be result from a field-induced antiferromagnetic ordering of the Sm and transition metal sublattices, as in $SmNi_4Si$ [40]. The magnetic transitions of $Sm_3Co_2Ge_3$ at T_N=51 K and T_m=10 K may correspond to an antiferromagnetic ordering of the Sm sublattice, while a positive value of the magnetic entropy change at 25 K may indicate an antiferromagnetic ordering of the Sm and Co sublattices. The proposed magnetic ordering of $Sm_3Co_2Ge_3$ should be investigated in the future.

5. Conclusion

Rare-earth '*R*2-2*R*1' clusters of the rare-earth *R*1 8*f* and *R*2 4*c* sublattices determine the magnetic ordering of the $Hf_3Ni_2Si_3$-type $Tb_3Ni_2Ge_3$ and $Tb_3Co_2Ge_3$. Similar field-sensitive antiferromagnetic structures are suggested in the $Hf_3Ni_2Si_3$-type rare-earth germanides with different magnetic space groups and propagation vectors, whereas $Hf_3Ni_2Si_3$-type silicides may show a similar field-sensitive ferro-antiferromagnetic ordering due to a suppression (distortion) of the unit cell and corresponding transformation of the '*R*2-2R1' clusters.

Acknowledgments

This work was supported by the Indo-Russian Fund for Basic Research through the project N° 15–53-45129-a and Russian Fund for Basic Research through the project N° 16-03-00666-a. This work supported by a ICDD (USA) grant N 05-07. - The unit cell data of $Sm_3Co_2Ge_3$, $Tb_3Co_2Ge_3$, $Er_3Co_2Ge_3$ and $Ho_3Ni_2Ge_3$ used with permission - ©JCPDS - International Centre for Diffraction Data. The Institute Laue Langevin is warmly acknowledged for the use of the neutron diffraction beam as well as the CNRS-CRG-instruments. S.K.M. thanks CAPES for the award of a fellowship, MEC and MCTI (Brazil) for financial support during the course of this work.

Appendix A. Supplementary material

Supplementary data associated with this article can be found in the online version at doi:10.1016/j.jmmm.2016.10.036.

References

[1] A.V. Morozkin, R. Nirmala, J. Yao, Y. Mozharivskyj, O. Isnard, J. Solid State Chem. 196 (2012) 93–99.
[2] A.V. Morozkin, A.V. Knotko, V.O. Yapaskurt, Fang Yuan, Y. Mozharivskyj, M. Pani, A. Provino, P. Manfrinetti, J. Solid State Chem. 225 (2015) 193–201.
[3] The Landolt-Börnstein Database – Materials Science Data for 250000 Substances, Springer Materials. ⟨http://www.springermaterials.com⟩.
[4] Pearson's Handbook of Crystallographic Data for Intermetallic Phases, 1985, American Society for Metals Metals Park, pp. 1–3.
[5] R. Welter, I. Ijjalli, G. Venturini, B. Malaman, J. Alloy. Compd. 257 (1997) 196–200.
[6] B. Chabot, N. Engel, E. Parthй, J. Less-Common Met. 96 (1984) 331–340.
[7] E.I. Gladyshevskii, B.Ya Kotur, Kristallografiya 23 (1978) 946–950.
[8] A.O. Oliynyk, Kadar Djama-Kayad, A. Mar, J. Alloy. Compd. 602 (2014) 130–134.
[9] V.Ya Markiv, E.A. Beloborodova, N.N. Belyavina, N.V. Alekseeva, Dopov. Akad. Nauk Ukr. (1993) 70–73.
[10] O.I. Bodak, O.Ya Oleksin, M.F. Fedyna, V.K. Pecharskii, Neorg. Mater. 28 (1992) 493–497.
[11] B.Ya Kotur, R.I. Andrusyak, Neorg. Mater. 27 (1991) 1433–1439.
[12] A.V. Morozkin, J. Yao, Yu Mozharivskyj, Intermetallics 21 (2012) 115–120.
[13] A.V. Morozkin, Intermetallics 25 (2012) 136–138.
[14] V.V. Pavlyuk, O.I. Bodak, Neorg. Mater. 28 (1992) 1119–1121.
[15] A.O. Oliynyk, S.S. Stoyko, A. Mar, J. Solid State Chem. 202 (2013) 241–249.
[16] O.L. Sologub, Yu.M. Prots', P.S. Salamakha, O.I. Bodak, J. Alloy. Compd. 209 (1994) 107–109.
[17] O.L. Sologub, Yu.M. Prots, P.S. Salamakha, O.I. Bodak, J. Stiepien-Damm, Pol. J. Chem. 69 (1995) 423–426.
[18] O.L. Sologub, K. Hiebl, P. Rogl, H. Noel, J. Alloy. Compd. 245 (1996) L13–L17.
[19] P. Salamakha, O. Sologub, J. Stiepien-Damm, A. Stash, Kristallografiya 41 (1996) 1135–1136.
[20] U.Ch Rodewald, R. Pottgen, Solid State Sci. 5 (2003) 487–493.
[21] O.I. Bodak, G.M. Koterlyn, in: Proceedings of the 6th Conference on Crystal Chemistry of Intermetallic Compounds, 1995, p. 26
[22] G.M. Koterlyn, O.I. Bodak, V.V. Pavlyuk, J. Stepien Damm, A. Pietraszko, J. Alloy. Compd. 291 (1999) 110–116.
[23] Yellow Book. ⟨www.ill.eu⟩.
[24] F. Izumi, R.A. Young (Ed.)The Rietveld Method, Oxford University Press, Oxford, 1993, p. 13.
[25] Bilbao Crystallographic Server (The Crystallographic Site at the Condensed Matter Physics Deptartment of the University of the Basque Country). ⟨http://www.crys.ehu.es⟩.
[26] R.A. Levy, Principles of Solid State Physics, Academic Press, NY (USA), 1968.
[27] A.M. Tishin, Y.L. Spichkin, The Magnetocaloric Effect and Its Applications, Institute of Physics Publishing, Bristol, Philadelphia, 2003, p. 480.
[28] J. Rodriguez-Carvajal, Physica B 192 (1993) 55–69.
[29] P.S. Kireev, Introduction to the Theory Group and It's Application in Solid State Physic, High School, Moscow, 1979 (in Russian).
[30] C.J. Bradley, A.P. Cracknell, The Mathematical Theory of Symmetry in Solids, Clarendon, Oxford, 1972.
[31] D.B.Litvin, Magnetic Group Tables, 1-, 2- and 3-Dimensional Magnetic Subperiodic Groups and Magnetic Space Groups, International Union of Crystallography, Reviewed by the IUCr Commission on Magnetic Structures, 2013, ISBN 978-0-9553602-2-0 doi:10.1107/9780955360220001.
[32] J. Emsley, The Elements, second edition, Clarendon press, Oxford, 1991.
[33] Fizicheskie velichiny (Physical Data). Handbook, Ed. by I.S. Grigor'ev, E.Z. Meilohov, Energoatomizdat, Moscow, 1994 (in Russian).
[34] S. Legvold, Chapter 3 Rare Earth Metals and Alloys, in: E.P. Wohlfarth (Ed.), Ferromagnetic Materials 1, North-Holland Publish. Comp., Amsterdam, 1980, pp. 183–295 (ISBN: 978-0-444-85311-0).
[35] G. André, F. Bourée, M. Kolenda, A. Oles, A. Pacyna, M. Pinot, W. Sikora, A. Szytula, J. Magn. Magn. Mater. 116 (1992) 375–385.
[36] P. Schobinger-Papamantellos, K.H.J. Buschow, T. Janssen, Mater. Sci. Forum 166–169 (1994) 479–486.
[37] L. Durivault, F. Bourée, B. Chevalier, G. André, J. Etourneau, O. Isnard, J. Magn. Magn. Mater. 232 (2001) 139–146.
[38] B. Chevalier, M. Pasturel, J.-L. Bobet, R. Decourt, J. Etourneau, O. Isnard, J. Sanchez Marcos, J. Rodriguez Fernandez, J. Alloy. Comp. 383 (2001) 4–9.
[39] A.V. Morozkin, A.V. Knotko, V.O. Yapaskurt, A. Provino, P. Manfrinetti, Jinlei Yao, Y. Mozharivskyj, Intermetallics 41 (2013) 70–75.
[40] Jinlei Yao, A.V. Morozkin, J. Solid State Chem. 230 (2015) 249–253.